



ELSEVIER

Available online at www.sciencedirect.com

SCIENCE @ DIRECT®

Computer Vision
and Image
Understanding

Computer Vision and Image Understanding 100 (2005) 312–329

www.elsevier.com/locate/cviu

Segmentation of tissue boundary evolution from brain MR image sequences using multi-phase level sets

Corina S. Drapaca^{a,*}, Valerie Cardenas^b, Colin Studholme^b

^a *Department of Applied Mathematics, University of Waterloo, 200 University Ave. West, Waterloo, Ont., Canada N2L 3G1*

^b *Department of Radiology, University of California in San Francisco, VA Medical Center(114Q), 4150 Clement Street, San Francisco, CA 94121, USA*

Received 9 June 2004; accepted 26 May 2005

Available online 20 July 2005

Abstract

In this paper, we focus on the automated extraction of the cerebrospinal fluid-tissue boundary, particularly around the ventricular surface, from serial structural MRI of the brain acquired in imaging studies of aging and dementia. This is a challenging segmentation problem because of the common occurrence of peri-ventricular lesions which locally alter the appearance of white matter. We examine a level set approach which evolves a 4D description of the ventricular surface over time. This has the advantage of allowing constraints on the contour in the temporal direction, improving the consistency of the extracted object over time. The 3D MR images of the entire brain are first aligned using global rigid registration. We then follow the approach proposed by Chan and Vese which is based on the Mumford and Shah model and implemented using the Osher and Sethian level set method. We have extended this to the 4D case to propagate a 4D contour toward the tissue boundaries through the evolution of a 5D implicit function. For convergence we use region-based information provided by the image rather than the gradient of the image. This model is then adapted to allow intensity

* Corresponding author.

E-mail addresses: csdrapaca@math.uwaterloo.ca (C.S. Drapaca), valerie@itsa.ucsf.edu (V. Cardenas), colin.studholme@ieee.org (C. Studholme).

contrast changes between time frames in the MRI sequence. Results on time sequences of 3D brain MR images are presented and discussed.

© 2005 Elsevier Inc. All rights reserved.

Keywords: MRI segmentation; PDE's; Level sets; Curve evolution; Edge detection; Active contours

1. Introduction

In recent years, brain magnetic resonance image segmentation established itself as an important research field, because of the increased need to correctly analyze and quantify brain anatomy and function. In this paper, we consider the problem of accurately extracting ventricular surface from serial structural MRI of the brain, in imaging studies of aging, and dementia. Extracting an accurate representation of the tissue-cerebrospinal fluid (CSF) boundary is a key step in evaluating tissue volume loss over time, which is important in the study of different neurodegenerative diseases. Specifically, accurately estimating the amount and location of tissue loss allows the tracking of a disease effect over time, providing a key to diagnosis and ultimately providing a direct quantitative measure of any treatment effect provided by drugs or other clinical interventions.

This image segmentation problem is challenging because of the common occurrence of peri-ventricular lesions in MRI of even normally aging subjects which locally alter the appearance of white matter surrounding the ventricular space. An example is illustrated in Fig. 1. This shows the expansion of the ventricular CSF region (dark) and contraction of surrounding white matter (bright), together with the development of a region (gray) of white matter lesion on the lateral surface of the ventricle. The changes in intensity of a given tissue in a temporal MRI sequence (that we can see, for example, in Fig. 1) are not only local, due to changes in tissue integrity, but also global, due to inherent scanner setup differences. In addition, because

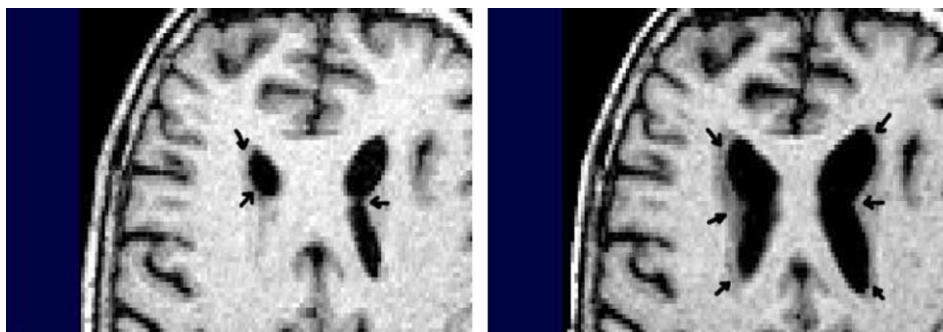


Fig. 1. Trans-axial slices through structural MRI of a subject with Alzheimer's disease, at two different time points showing the expansion of the ventricle and growth of peri-ventricular white matter lesions (the arrows point to the lesions).

of the limited resolution of the MRI data, the CSF structures of the ventricle are not necessarily linked into one connected CSF structure. This topology may change as tissue surrounding the ventricles is lost over time. We therefore require a segmentation process to allow the delineation of CSF from white matter that may have an unknown and temporally varying topology. In what follows, we will give a brief presentation of a class of segmentation methods that we believe may work for this problem and illustrate its use on example and synthetic image data.

1.1. Brief review

Due to the important role that image segmentation can play in clinical procedures, many segmentation methods have been developed in recent years. Among them, those approaches based on the evolution of active contours have generated much interest. *Active contours* are hyper-surfaces that propagate in the direction of intensity gradient to recover object boundaries. The active contours can be either *parametric* or *geometric*. The classical parametric contours [9,15] are based on the minimization of an energy functional that takes a minimum when contours are smooth and reside on the object boundaries. They are represented explicitly as parametrized hyper-surfaces using the local Lagrangian method. However, this model is limited because first, the external forces resulting from this model are conservative forces (i.e., they are gradients of scalar potential functions), second, re-parametrization is required to explicitly handle topological changes, and third, the initialization must be close to the desired location to avoid oscillations and instabilities which inevitably appear during the evolution process. To allow for more general external forces (like region-based forces) to act on the contour, Xu et al. [30,31] formulated parametric active contours directly from Newton's law of motion but the handling of topological changes are still a drawback of the method.

Geometric active contours are represented implicitly as level sets of signed distance functions which evolve according to a global, Eulerian method [23,16,17,4,18,11–13]. They can be described by level sets of higher-dimensional functions, which offer a range of advantages including independence from the choice of parametrization, the ability to permit topological changes and the availability of stable and efficient numerical solution schemes. (It is worthwhile mentioning here that there is another image segmentation technique very similar to the level set method called *fuzzy connectedness*; for a tutorial on this topic see [27].)

It has been shown [3,5,6,28,29,19] that the geometric active contours are minimizers of some energy functionals which control the smoothness of the contours and attract the contours toward the objects in the image. More generally, if the minimization of the energy functional is based on a geodesic computation in a Riemannian space, according to a metric induced by the given image, the corresponding geometric active contours are also called *geodesic active contours* [5,3]. Taking into account the apparent similarity between parametric and geometric active contours, Xu et al. [30,31] found a mathematical relationship between these two active contour formulations. This relationship helps, for example, in improving the robustness of a geometric active contour during the segmentation process both to noise and to weak

edges. The so-called leaking problem, which results from weak edges, is solved by introducing region-based forces in the evolution equation of a geometric active contour.

To segment images using active contour models, we need to prescribe an initial contour and an energy functional. However, one of the fundamental issues is the selection of a suitable energy functional whose minima will stop the given contour on the underlying anatomical boundary of interest. Usually, an edge-detector function, depending on the gradient of the image, is implemented inside the energy functional and it should work as a stopping criteria. The most used edge-detector function is a positive and decreasing function of the gradient of the image which is zero at the boundaries. A Gaussian filter is applied to the image to enhance its boundaries and hence make the image gradients stronger. Because the discrete gradients are bounded, the edge-detector (or stopping) function is never zero on the edges and hence the contour may pass through the boundary. One way to deal with weak edges is, as we mentioned before, to add region-based forces into the energy functional [30,31,8]. Also, in the classical level set theory, the initial contour must be either totally outside or inside of the object to be segmented because the method allows only one-way contour evolutions: shrinking or growing of the initial contour [23,16]. This may cause the non-detection of several objects and holes. Thus, the energy functional has to be again modified in such a way that it allows for arbitrary initial contour positions [2,1,10].

Recently, Chan and Vese proposed the so-called *geometric active contours without edges* whose energy functional is based on the Mumford and Shah model [6,28,29]. To stop the evolving hyper-surface on the boundaries of interest, this model uses region-based information provided by the image rather than the gradient of the image. Thus, not only does this model have all the attractive features of the geometric active contours mentioned before but also it is more robust in the presence of noise and weak edges. The model can detect objects both with and without gradient, with weak edges, discontinuous boundaries or with holes. In addition, the initial moving interface can be anywhere in the image. All these advantages make this model particularly suited to our segmentation problem and, therefore, we decided to implement a 4D adaptation of the method that Chan and Vese explored in two dimensions. As it was shown in [28], by using at least two level set functions to represent the evolving interface instead of just one, not only does the algorithm become faster, but also any existing triple junctions (junctions between three tissue classes, such as white matter, gray matter, and cerebrospinal fluid) in the image can be correctly detected. However, due to lack of uniqueness among minimizers, the method becomes more sensitive to the initial contour position on more complicated images.

For simplicity, we considered the case of a piecewise-constant approximation of the image function in this multi-phase level set framework. This method accepts a set of globally rigidly aligned volumetric images and extracts a set of closed contours corresponding to evolving boundaries with consistent contrast over time within the image sequence. The algorithm requires an initial boundary and one global parameter which has a scaling role determining the overall size of objects to be extracted.

We first extended the multi-phase model of Chan and Vese to the 4D case which can be applied only to 4D data in which there is no intensity change from one time point to the next. To apply this 4D algorithm to a sequence of high resolution time series T1 weighted MR images, we had to modify the model such that it will take into account the intensity changes in the temporal sequence and the smoothness differences between the three spatial domain and the temporal one. We have explored the use of this modified algorithm to extract ventricular surfaces from the temporal sequence. Experiments were conducted to examine final contour and convergence characteristics of the algorithm to different starting conditions and parameter values. From our knowledge, this is the first time that this segmentation technique has been used to extract objects from time sequences of real image data. The results obtained provide visually accurate ventricular boundaries.

The present paper was structured as follows. In Section 2 we give a brief presentation of the extended multi-phase level set model to the 4D case and introduce a novel adaptation of this model to time series MRI. The numerical algorithm we used and our results follow in the next two sections. The paper ends with a section of conclusions and future work.

2. Method

In this section we give two modifications of the multi-phase level set model of Chan and Vese [28]. One is the straightforward extension of the Chan and Vese model to the 4D case to segment 3D image sequences with no intensity changes in the temporal direction. The second adaptation is a 4D multi-phase model for time series of images where tissue intensities change from one time point to another.

2.1. Basic multi-phase level set method

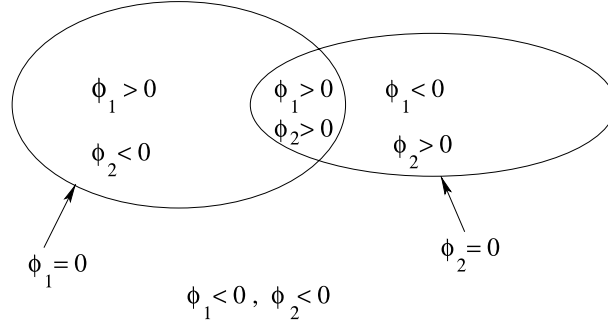
In what follows we briefly present the extension of the 4-phase piecewise constant active contour model without edges [28] to the 4D case. With this method we can represent four segments or classes with complex topologies (such as triple junctions) in an efficient way using only two level set functions and there is no vacuum or overlap among the phases.

Let $\Omega \subset \mathbf{R}^4$ be a bounded open set with $\partial\Omega$ its boundary and $u_0 : \bar{\Omega} \rightarrow \mathbf{R}$ be a given image. Let $\Gamma(\tau)$ be a closed moving interface in \mathbf{R}^4 of co-dimension 1 [23,20]. We consider that, at any time τ , the interface Γ is described implicitly by the union of the zero level sets of two higher-dimensional functions (*level set functions*) $\phi_\alpha : \Omega \times \mathbf{R}^+ \rightarrow \mathbf{R}$, $\alpha = 1, 2$

$$\Gamma(\tau) = \{\vec{v} \in \Omega \mid \phi_1(\vec{v}, \tau) = 0\} \cup \{\vec{v} \in \Omega \mid \phi_2(\vec{v}, \tau) = 0\},$$

where we denoted by $\vec{v} = (x, y, z, t)$.

Typically, the level set functions ϕ_α are chosen to be signed Euclidean distances to the interface $\Gamma(\tau)$ as shown in Fig. 2. Let $H(\phi_\alpha)$ be the Heaviside function defined by:

Fig. 2. $\Gamma(\tau)$ partition Ω into four phases [28].

$H(\phi_\alpha) = 1$ if $\phi_\alpha \geq 0$, and $H(\phi_\alpha) = 0$ if $\phi_\alpha < 0$. Each class or phase is formed by those points $\vec{v} \in \Omega$ having the same value $H(\phi_\alpha)$, $\alpha = 1, 2$. This definition of the phases insures that each point of Ω belongs to one and only one class and hence there is no vacuum or overlap among the phases.

If we assume that the image intensity does not change from one time point to another then we can approximate the image function u with a piecewise-constant function:

$$u = c_{11}H(\phi_1)H(\phi_2) + c_{10}H(\phi_1)(1 - H(\phi_2)) + c_{01}(1 - H(\phi_1))H(\phi_2) + c_{00}(1 - H(\phi_1))(1 - H(\phi_2)), \quad (1)$$

where c_{11} , c_{01} , c_{10} , and c_{00} are positive constants. In this case the Mumford and Shah-like functional whose minimum will give us the segmentation of the image in four classes is:

$$\begin{aligned} \mathcal{F}(c_{11}, c_{01}, c_{10}, c_{00}, \phi_1, \phi_2) &= \int_{\Omega} (u_0 - c_{11})^2 H(\phi_1)H(\phi_2) \, d\vec{v} \\ &+ \int_{\Omega} (u_0 - c_{10})^2 H(\phi_1)(1 - H(\phi_2)) \, d\vec{v} \\ &+ \int_{\Omega} (u_0 - c_{01})^2 (1 - H(\phi_1))H(\phi_2) \, d\vec{v} \\ &+ \int_{\Omega} (u_0 - c_{00})^2 (1 - H(\phi_1))(1 - H(\phi_2)) \, d\vec{v} \\ &+ v \int_{\Omega} (|\nabla H(\phi_1)| + |\nabla H(\phi_2)|) \, d\vec{v}, \end{aligned} \quad (2)$$

where $v < 0$ is a scale parameter which has to be given. We denoted by $d\vec{v} = dx \, dy \, dz \, dt$.

Minimizing (2) with respect to c_{11} , c_{01} , c_{10} , c_{00} , ϕ_1 , and ϕ_2 yields the following Euler–Lagrange equations evolving ϕ_1 and ϕ_2 embedded in a dynamic scheme:

$$\begin{aligned}
 \frac{\partial \phi_1}{\partial \tau} &= \delta(\phi_1) \left\{ v \operatorname{div} \left(\frac{\nabla \phi_1}{|\nabla \phi_1|} \right) - \left[((u_0 - c_{11})^2 - (u_0 - c_{01})^2) H(\phi_2) \right. \right. \\
 &\quad \left. \left. + ((u_0 - c_{10})^2 - (u_0 - c_{00})^2) (1 - H(\phi_2)) \right] \right\}, \\
 \frac{\partial \phi_2}{\partial \tau} &= \delta(\phi_2) \left\{ v \operatorname{div} \left(\frac{\nabla \phi_2}{|\nabla \phi_2|} \right) - \left[((u_0 - c_{11})^2 - (u_0 - c_{10})^2) H(\phi_1) \right. \right. \\
 &\quad \left. \left. + ((u_0 - c_{01})^2 - (u_0 - c_{00})^2) (1 - H(\phi_1)) \right] \right\}
 \end{aligned} \tag{3}$$

where $\delta(\phi_\alpha)$, $\alpha = 1, 2$ is the Dirac distribution and

$$\begin{aligned}
 c_{11} &= \frac{\int_{\Omega} u_0 H(\phi_1) H(\phi_2) \, d\vec{v}}{\int_{\Omega} H(\phi_1) H(\phi_2) \, d\vec{v}}, & c_{10} &= \frac{\int_{\Omega} u_0 H(\phi_1) (1 - H(\phi_2)) \, d\vec{v}}{\int_{\Omega} H(\phi_1) (1 - H(\phi_2)) \, d\vec{v}}, \\
 c_{01} &= \frac{\int_{\Omega} u_0 (1 - H(\phi_1)) H(\phi_2) \, d\vec{v}}{\int_{\Omega} (1 - H(\phi_1)) H(\phi_2) \, d\vec{v}}, & c_{00} &= \frac{\int_{\Omega} u_0 (1 - H(\phi_1)) (1 - H(\phi_2)) \, d\vec{v}}{\int_{\Omega} (1 - H(\phi_1)) (1 - H(\phi_2)) \, d\vec{v}}
 \end{aligned} \tag{4}$$

are the means of u_0 corresponding to the four phases.

Eq. (3) are governed by both mean curvature and jump of the data energy terms across the boundary. Suitable initial conditions $\phi_\alpha(x, y, z, t, 0)$, $\alpha = 1, 2$ are required to solve these equations.

2.2. Adaptation to time series MRI

A 4D MRI sequence is a combination of multiple 3D independent structural MRI data sets acquired at different time points. As a result there are two important differences between a MRI temporal sequence and an ideal 4D image. First, in this image the intensity of a given tissue will vary from one time point to the next. This will occur globally because of scanner setup differences and locally because of changes in tissue integrity as lesions evolve over time as shown in Fig. 1. Second, the complexities of an anatomical boundary in spatial and temporal directions are not physically comparable; therefore, for example, a cortical surface may be highly curved in the three spatial domain, but gently curved in the temporal domain where the brain is changing little between time points (as is the case with many serial imaging studies). We have therefore developed two modifications to the above presented model. One deals with the intensity changes. The other modification is in the definition of the gradient operator in space and time.

2.2.1. Intensity model

As we mentioned before, relation (1) does not take into account the intensity changes in the temporal direction and, therefore, is not suited for the segmentation of a 4D MRI sequence. To solve this problem without losing the simplicity of the previous model, we assume now that, at each time point, the image u is a piecewise-constant function of form (1). Thus,

$$u = c_{11}(t)H(\phi_1)H(\phi_2) + c_{10}(t)H(\phi_1)(1 - H(\phi_2)) + c_{01}(t)(1 - H(\phi_1)) \times H(\phi_2) + c_{00}(t)(1 - H(\phi_1))(1 - H(\phi_2)),$$

where

$$c_{ab}(t) = c_{ab}^0 + \sum_{l=1}^L (c_{ab}^l - c_{ab}^{l-1})H(t - l), \quad a, b \in \{0, 1\} \tag{5}$$

with $c_{ab}^l, a, b \in \{0, 1\}, l = \overline{0, L}$ positive constants and L the total number of time points. The expression of the energy functional and the Euler–Lagrange equations are still given by (2) and, respectively (3), where the positive constants are replaced with expressions (5). In this case the positive constants $c_{ab}^l, a, b \in \{0, 1\}, l = \overline{0, L}$ are given by:

$$\begin{aligned} c_{11}^l &= \frac{\int_{\Omega} u_0(H(t - l) - H(t - (l + 1)))H(\phi_1)H(\phi_2) \, d\vec{v}}{\int_{\Omega} (H(t - l) - H(t - (l + 1)))H(\phi_1)H(\phi_2) \, d\vec{v}}, \\ c_{10}^l &= \frac{\int_{\Omega} u_0(H(t - l) - H(t - (l + 1)))H(\phi_1)(1 - H(\phi_2)) \, d\vec{v}}{\int_{\Omega} (H(t - l) - H(t - (l + 1)))H(\phi_1)(1 - H(\phi_2)) \, d\vec{v}}, \\ c_{01}^l &= \frac{\int_{\Omega} u_0(H(t - l) - H(t - (l + 1)))(1 - H(\phi_1))H(\phi_2) \, d\vec{v}}{\int_{\Omega} (H(t - l) - H(t - (l + 1)))(1 - H(\phi_1))H(\phi_2) \, d\vec{v}}, \\ c_{00}^l &= \frac{\int_{\Omega} u_0(H(t - l) - H(t - (l + 1)))(1 - H(\phi_1))(1 - H(\phi_2)) \, d\vec{v}}{\int_{\Omega} (H(t - l) - H(t - (l + 1)))(1 - H(\phi_1))(1 - H(\phi_2)) \, d\vec{v}}, \end{aligned} \tag{6}$$

and are the means of u_0 corresponding to the four phases at each time step l .

2.2.2. Smoothness model

In terms of the 4D structure present in an MRI sequence, the spatial and temporal dimensions cannot be directly equated. Specifically, we know that, with respect to the sampling units in each dimension, the anatomical boundaries are much more highly curved in the three spatial dimensions, than in the temporal dimension between time frames. In other words, we know that the changes between time points are small. We can use this in the algorithm directly to assist tracking the evolution of a boundary in the temporal dimension as tissue intensities change. In essence, we wish the spatial partitioning in a given frame to be constrained by the partitioning of neighboring boundaries in time. This is achieved within the surface evolution framework by imposing constraints on the curvature of the surface, i.e., by introducing weights into the definition of the gradient operator, such that

$$\nabla \phi_{\alpha} = \left(w_x \frac{\partial \phi_{\alpha}}{\partial x}, w_y \frac{\partial \phi_{\alpha}}{\partial y}, w_z \frac{\partial \phi_{\alpha}}{\partial z}, w_t \frac{\partial \phi_{\alpha}}{\partial t} \right), \alpha = 1, 2, \tag{7}$$

where the weights $w_x, w_y, w_z,$ and w_t are positive parameters which need to be defined. These allow us to control the smoothness of the boundary in each direction. For example, a larger value for w_t relative to $w_x, w_y,$ and w_z means that the boundary is forced to be smoother in time than space relative to the image sampling intervals in

each direction. This means that, at a given time point, the boundary location is determined by the image structure at that time point, together with that in its neighbors in time. This provides an important geometrical prior to address the uncertainty which can arise in the evolution of diffuse lesion boundaries. In practice we know the relative size of the three spatial weights w_x , w_y , and w_z , derived from the known voxel dimensions of the MRI data. The main parameter to be defined is the relative size of weight w_t with respect to the spatial weights.

2.3. Numerical algorithm

As in [6,28,29], we approximate the Heaviside function H and the Dirac distribution δ by:

$$H_\epsilon(\phi_\alpha(\vec{v}, \tau)) = \frac{1}{2} \left(1 + \frac{2}{\pi} \arctan \left(\frac{\phi_\alpha(\vec{v}, \tau)}{\epsilon} \right) \right),$$

$$\delta_\epsilon(\phi_\alpha(\vec{v}, \tau)) = \frac{1}{\pi} \frac{\epsilon}{\epsilon^2 + (\phi_\alpha(\vec{v}, \tau))^2}, \quad \alpha = 1, 2$$

with ϵ a positive small parameter.

These approximations and regularizations H_ϵ and δ_ϵ converge to the real H and δ as $\epsilon \rightarrow 0$. It is believed that using H_ϵ and δ_ϵ helps in computing a global minimizer [6]. We have to keep in mind though that, because the Mumford and Shah energy functional is non-convex and because we use the gradient descent method to solve the Euler–Lagrange equations, this model can find only *local* minimizers. Therefore, we can only hope to find the *best possible local* minimizer.

Let Δx , Δy , and Δz be the space steps, Δt be the time step and $\Delta \tau$ be the evolution time step of the level set functions. We denote by $x_i = i\Delta x$, $i = \overline{0, I}$, $y_j = j\Delta y$, $j = \overline{0, J}$, $z_k = k\Delta z$, $k = \overline{0, K}$, $t_l = l\Delta t$, $l = \overline{0, L}$, $\phi_{\alpha_{ijkl}}^n = \phi_\alpha(x_i, y_j, z_k, t_l, \tau_n)$, $\alpha = 1, 2$, and $u_{0_{ijkl}} = u_0(x_i, y_j, z_k, t_l)$.

The algorithm steps are as follows [28]:

- (1) Initialize $\phi_\alpha(x, y, z, t, 0)$, $\alpha = 1, 2$ for $n = 0$.
- (2) Compute the means $c_{11}^n, c_{10}^n, c_{01}^n, c_{00}^n$ using formulas (4) or (6).
- (3) Solve the discrete Eq. (3) (with $c_{11}^n, c_{10}^n, c_{01}^n, c_{00}^n$ given by (4) or (5) and (6) using a semi-implicit finite difference scheme and get $\phi_{1_{ijkl}}^{n+1}, \phi_{2_{ijkl}}^{n+1}$. The gradient operator is given by (7). The numerical scheme looks as follows. Let $\Delta x = \Delta x/w_x$, $\Delta y = \Delta y/w_y$, $\Delta z = \Delta z/w_z$, and $\Delta t = \Delta t/w_t$. We denote by:

$$A_{\alpha_1} = \left[\left(\frac{\phi_{\alpha_{i+1,jkl}}^n - \phi_{\alpha_{ijkl}}^n}{\Delta x} \right)^2 + \left(\frac{\phi_{\alpha_{i,j+1,kl}}^n - \phi_{\alpha_{i,j-1,kl}}^n}{2\Delta y} \right)^2 + \left(\frac{\phi_{\alpha_{ij,k+1,l}}^n - \phi_{\alpha_{ij,k-1,l}}^n}{2\Delta z} \right)^2 + \left(\frac{\phi_{\alpha_{ijk,l+1}}^n - \phi_{\alpha_{ijk,l-1}}^n}{2\Delta t} \right)^2 \right]^{-\frac{1}{2}},$$

$$A_{\alpha_2} = \left[\left(\frac{\phi_{\alpha_{ijkl}}^n - \phi_{\alpha_{i-1,jkl}}^n}{\Delta x} \right)^2 + \left(\frac{\phi_{\alpha_{i-1,j+1,kl}}^n - \phi_{\alpha_{i-1,j-1,kl}}^n}{2\Delta y} \right)^2 \right. \\ \left. + \left(\frac{\phi_{\alpha_{i-1,j,k+1,l}}^n - \phi_{\alpha_{i-1,j,k-1,l}}^n}{2\Delta z} \right)^2 + \left(\frac{\phi_{\alpha_{i-1,jk,l+1}}^n - \phi_{\alpha_{i-1,jk,l-1}}^n}{2\Delta t} \right)^2 \right]^{-\frac{1}{2}},$$

$$A_{\alpha_3} = \left[\left(\frac{\phi_{\alpha_{i+1,jkl}}^n - \phi_{\alpha_{i-1,jkl}}^n}{2\Delta x} \right)^2 + \left(\frac{\phi_{\alpha_{i,j+1,kl}}^n - \phi_{\alpha_{ijkl}}^n}{\Delta y} \right)^2 \right. \\ \left. + \left(\frac{\phi_{\alpha_{ij,k+1,l}}^n - \phi_{\alpha_{ij,k-1,l}}^n}{2\Delta z} \right)^2 + \left(\frac{\phi_{\alpha_{ijk,l+1}}^n - \phi_{\alpha_{ijk,l-1}}^n}{2\Delta t} \right)^2 \right]^{-\frac{1}{2}},$$

$$A_{\alpha_4} = \left[\left(\frac{\phi_{\alpha_{i+1,j-1,kl}}^n - \phi_{\alpha_{i-1,j-1,kl}}^n}{2\Delta x} \right)^2 + \left(\frac{\phi_{\alpha_{ijkl}}^n - \phi_{\alpha_{i,j-1,kl}}^n}{\Delta y} \right)^2 \right. \\ \left. + \left(\frac{\phi_{\alpha_{i,j-1,k+1,l}}^n - \phi_{\alpha_{i,j-1,k-1,l}}^n}{2\Delta z} \right)^2 + \left(\frac{\phi_{\alpha_{i,j-1,k,l+1}}^n - \phi_{\alpha_{i,j-1,k,l-1}}^n}{2\Delta t} \right)^2 \right]^{-\frac{1}{2}},$$

$$A_{\alpha_5} = \left[\left(\frac{\phi_{\alpha_{i+1,jkl}}^n - \phi_{\alpha_{i-1,jkl}}^n}{2\Delta x} \right)^2 + \left(\frac{\phi_{\alpha_{i,j+1,kl}}^n - \phi_{\alpha_{i,j-1,kl}}^n}{2\Delta y} \right)^2 \right. \\ \left. + \left(\frac{\phi_{\alpha_{ij,k+1,l}}^n - \phi_{\alpha_{ijkl}}^n}{\Delta z} \right)^2 + \left(\frac{\phi_{\alpha_{ijk,l+1}}^n - \phi_{\alpha_{ijk,l-1}}^n}{2\Delta t} \right)^2 \right]^{-\frac{1}{2}},$$

$$A_{\alpha_6} = \left[\left(\frac{\phi_{\alpha_{i+1,j,k-1,l}}^n - \phi_{\alpha_{i-1,j,k-1,l}}^n}{2\Delta x} \right)^2 + \left(\frac{\phi_{\alpha_{i,j+1,k-1,l}}^n - \phi_{\alpha_{i,j-1,k-1,l}}^n}{2\Delta y} \right)^2 \right. \\ \left. + \left(\frac{\phi_{\alpha_{ijkl}}^n - \phi_{\alpha_{ij,k-1,l}}^n}{\Delta z} \right)^2 + \left(\frac{\phi_{\alpha_{ij,k-1,l+1}}^n - \phi_{\alpha_{ij,k-1,l-1}}^n}{2\Delta t} \right)^2 \right]^{-\frac{1}{2}},$$

$$A_{\alpha_7} = \left[\left(\frac{\phi_{\alpha_{i+1,jkl}}^n - \phi_{\alpha_{i-1,jkl}}^n}{2\Delta x} \right)^2 + \left(\frac{\phi_{\alpha_{i,j+1,kl}}^n - \phi_{\alpha_{i,j-1,kl}}^n}{2\Delta y} \right)^2 \right. \\ \left. + \left(\frac{\phi_{\alpha_{ij,k+1,l}}^n - \phi_{\alpha_{ij,k-1,l}}^n}{2\Delta z} \right)^2 + \left(\frac{\phi_{\alpha_{ijk,l+1}}^n - \phi_{\alpha_{ijkl}}^n}{\Delta t} \right)^2 \right]^{-\frac{1}{2}},$$

$$A_{\alpha_8} = \left[\left(\frac{\phi_{\alpha_{i+1,jk,l-1}}^n - \phi_{\alpha_{i-1,jk,l-1}}^n}{2\Delta x} \right)^2 + \left(\frac{\phi_{\alpha_{i,j+1,k,l-1}}^n - \phi_{\alpha_{i,j-1,k,l-1}}^n}{2\Delta y} \right)^2 + \left(\frac{\phi_{\alpha_{ij,k+1,l-1}}^n - \phi_{\alpha_{ij,k-1,l-1}}^n}{2\Delta z} \right)^2 + \left(\frac{\phi_{\alpha_{ijkl}}^n - \phi_{\alpha_{ijkl-1}}^n}{\Delta t} \right)^2 \right]^{\frac{1}{2}},$$

$$A_\alpha = 1 + v\Delta\tau\delta_\epsilon \left(\phi_{\alpha_{ijkl}}^n \right) \left[\frac{1}{\Delta x^2} (A_{\alpha_1} + A_{\alpha_2}) + \frac{1}{\Delta y^2} (A_{\alpha_3} + A_{\alpha_4}) + \frac{1}{\Delta z^2} (A_{\alpha_5} + A_{\alpha_6}) + \frac{1}{\Delta t^2} (A_{\alpha_7} + A_{\alpha_8}) \right], \quad \alpha = 1, 2.$$

Then:

$$\begin{aligned} \phi_{\alpha_{ijkl}}^{n+1} = & \frac{1}{A_\alpha} \left\{ v\Delta\tau\delta_\epsilon \left(\phi_{\alpha_{ijkl}}^n \right) \right. \\ & \times \left[\frac{1}{\Delta x^2} \left(A_{\alpha_1} \phi_{\alpha_{i+1,jkl}}^n + A_{\alpha_2} \phi_{\alpha_{i-1,jkl}}^n \right) + \frac{1}{\Delta y^2} \left(A_{\alpha_3} \phi_{\alpha_{i,j+1,kl}}^n + A_{\alpha_4} \phi_{\alpha_{i,j-1,kl}}^n \right) \right. \\ & \left. + \frac{1}{\Delta z^2} \left(A_{\alpha_5} \phi_{\alpha_{ij,k+1,l}}^n + A_{\alpha_6} \phi_{\alpha_{ij,k-1,l}}^n \right) + \frac{1}{\Delta t^2} \left(A_{\alpha_7} \phi_{\alpha_{ijk,l+1}}^n + A_{\alpha_8} \phi_{\alpha_{ijk,l-1}}^n \right) \right] \\ & - \left[\left((u_{0_{ijkl}} - c_{11}^n)^2 - (u_{0_{ijkl}} - c_{10}^n)^2 \right) H \left(\phi_{\beta_{ijkl}}^n \right) + \left((u_{0_{ijkl}} - c_{01}^n)^2 \right. \right. \\ & \left. \left. - (u_{0_{ijkl}} - c_{00}^n)^2 \right) \left(1 - H \left(\phi_{\beta_{ijkl}}^n \right) \right) \right] + \phi_{\alpha_{ijkl}}^n \left. \right\}, \end{aligned}$$

$$\alpha, \beta = 1, 2, \quad \alpha \neq \beta, \quad i = \overline{0, I}, \quad j = \overline{0, J}, \quad k = \overline{0, K}, \quad l = \overline{0, L}$$

with the following boundary conditions:

$$\begin{aligned} \phi_{\alpha_{-1,jkl}}^n &= \phi_{\alpha_{0,jkl}}^n, \phi_{\alpha_{i,-1,kl}}^n = \phi_{\alpha_{i,0,kl}}^n, \phi_{\alpha_{ij,-1,l}}^n = \phi_{\alpha_{ij,0,l}}^n, \\ \phi_{\alpha_{ijk,-1}}^n &= \phi_{\alpha_{ijk,0}}^n, \phi_{\alpha_{i+1,jkl}}^n = \phi_{\alpha_{ijkl}}^n, \phi_{\alpha_{i,j+1,kl}}^n = \phi_{\alpha_{ijkl}}^n, \\ \phi_{\alpha_{ij,K+1,l}}^n &= \phi_{\alpha_{ijkl}}^n, \phi_{\alpha_{ij,k,L+1}}^n = \phi_{\alpha_{ijkl}}^n, \quad \alpha = 1, 2. \end{aligned}$$

- (4) Check if the difference between the energy functional (2) (with $c_{11}^n, c_{10}^n, c_{01}^n, c_{00}^n$ given by (4) or (5) and (6) evaluated at n and the energy functional evaluated at $n - 1$, normalized by the energy evaluated at $n - 1$, is less than a given small threshold h . If yes, then the steady state solution was found and we stop. If not, $n = n + 1$ and we go back to step 1.

The values of $v, w_x, w_y, w_z,$ and w_t are the only parameters to be specified in the model.

3. Results

3.1. Test data

We tested the proposed method on two types of 4D images: one containing synthetic data and the other one made of real data. The synthetic image was an image

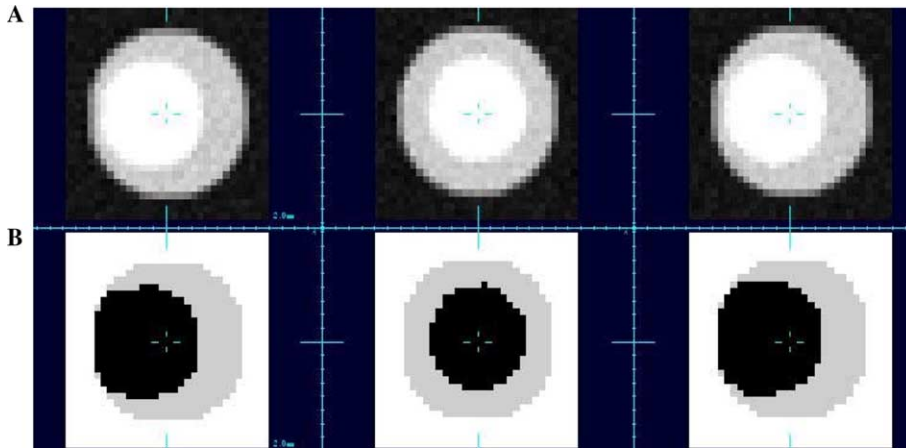


Fig. 3. Three orthogonal cuts (left to right) through the synthetic image volume at the first time point: original image (A), final segmentation (B).

sequence of 32 time points constructed by taking an analytic model of a pair of nested spheres and applying a random free form (B-Spline) deformation velocity field. This created a sequence of smoothly varying 3D structures that were then fed into a simple imaging model which simulated the effects of independent Gaussian noise and point spread function to create image volumes with noise and resolution comparable to an MRI sequence. At each time point the image has $32 \times 32 \times 32$ voxels with resolution $1 \times 1 \times 1$ mm as shown in Fig. 3A.

The second set of data we analyzed comes from a sequence of high resolution T1-weighted MR images of a subject with Alzheimer's disease acquired at intervals of approximately 1 year. The first MRI scan was used as a reference and each of the remaining MRI's was rigidly aligned to that using a multi-resolution maximization of normalized mutual information [24]. The rigidly aligned MRI volumes, each having $145 \times 156 \times 108$ voxels with resolution $0.9765 \times 0.9765 \times 1.4085$ mm were then composed into a single 4D data set for analysis. In MRI data such as this the intensity of the same tissue type varies from one time point to the next due to differences in the scanner configuration and also localized changes in the tissue integrity between time points.

3.2. Experimental results

Using both synthetic and serial MR images, experimental evaluation indicated suitable common algorithm parameters as follows. The evolution time step $\Delta\tau = 0.001$, the Heaviside and Dirac parameter $\epsilon = 1$, the scale parameter $\nu = 80$. The weights determining the relative smoothness in each axis were selected by experimentation to be $w_x = w_y = w_z = 1$, and $w_t = 8$. Due to inherent differences between the size and resolution of the synthetic and real data, we used two different stopping thresholds: $h = 0.005$ for the synthetic data and $h = 0.001$ for the 4D MRI sequence.

3.2.1. Synthetic data

The initial level set hyper-surfaces are two 4D cylinders of arbitrary positions such that one is inside the other and the inner cylinder is much smaller than the outer one. The results obtained using the above mentioned set of parameters are shown in Figs. 3 and 4. A rendering of the evolution of the synthetic data in 3D is shown in Fig. 5.

3.2.2. Serial MRI data

For this image we used again two 4D cylinders as initial level set hyper-surfaces. Our primary aim was to identify the CSF-tissue boundary of the ventricular system, but we evolved the level sets to partition the entire head. Taking into account the specific geometry of the brain, the two hyper-surfaces were both centered in the middle of the image such that one of the two interfaces is much smaller and entirely contained inside the other.

The results for the first and last time points are shown in Figs. 6 and 7. As we can see from the last rows of Figs. 6 and 7, which shows the contours of the segmented ventricles over the initial image, our model provides visually accurate ventricular boundaries, correctly separating the diffuse lesion around the ventricles from CSF (Fig. 7), together with many of the the white and gray matter boundaries in the cortex.

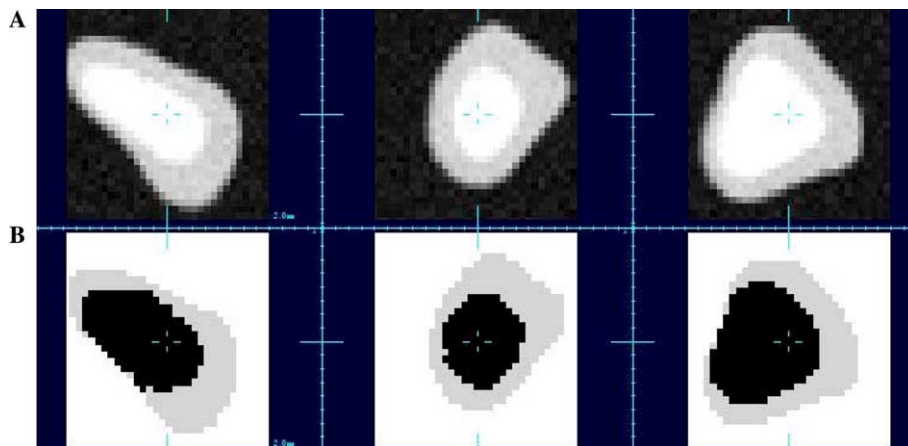


Fig. 4. Three orthogonal cuts (left to right) through the synthetic image volume at the last time point: original image (A), final segmentation (B).



Fig. 5. Evolution of the 3D surfaces for the synthetic image volume at the last time point, showing first (left) to fifth (right) iteration from initial spheres. (The two separate surfaces are shown in different colors.)

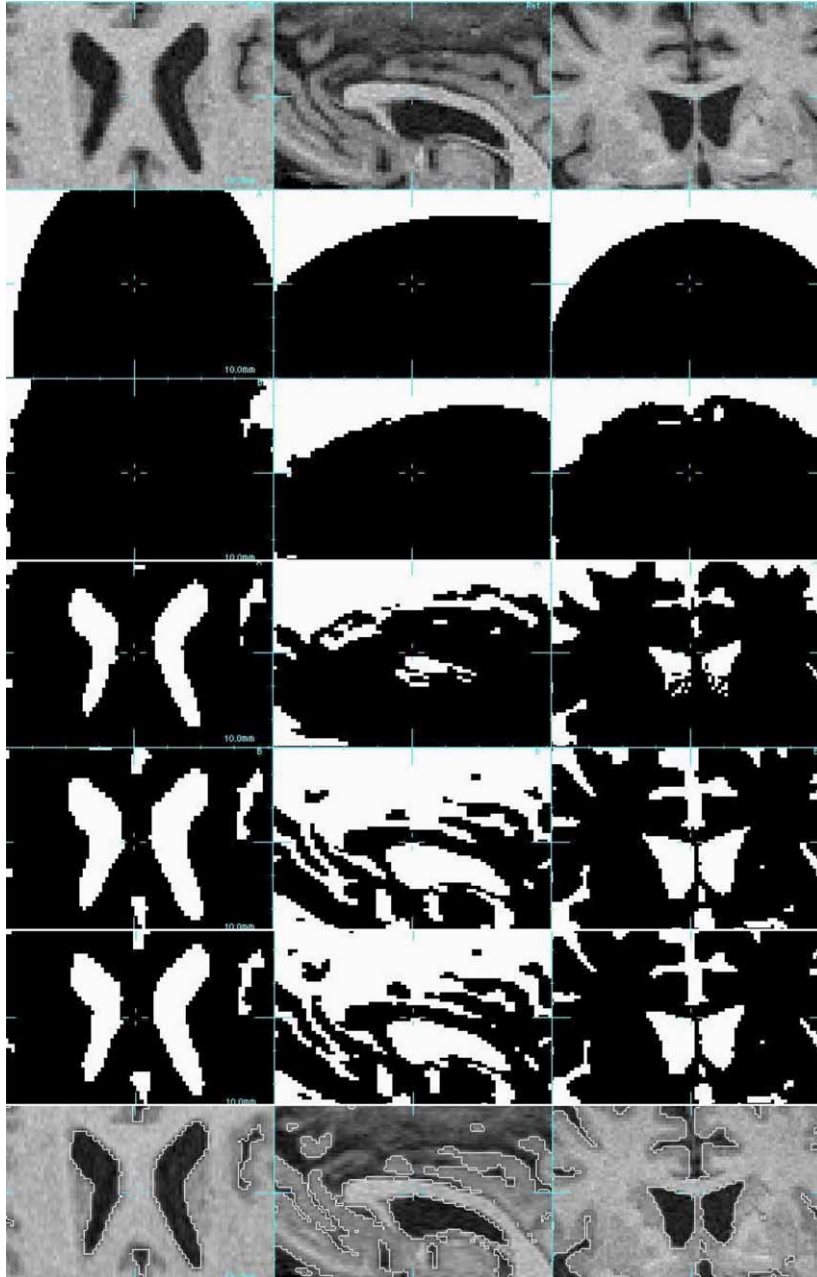


Fig. 6. Trans-axial (left), sagittal (middle), and coronal (right) slices through the: raw time point 1 image (first row), intermediate segmentation results and the final segmented CSF region (second to sixth row), tissue-CSF contour over the time point 1 image (last row).

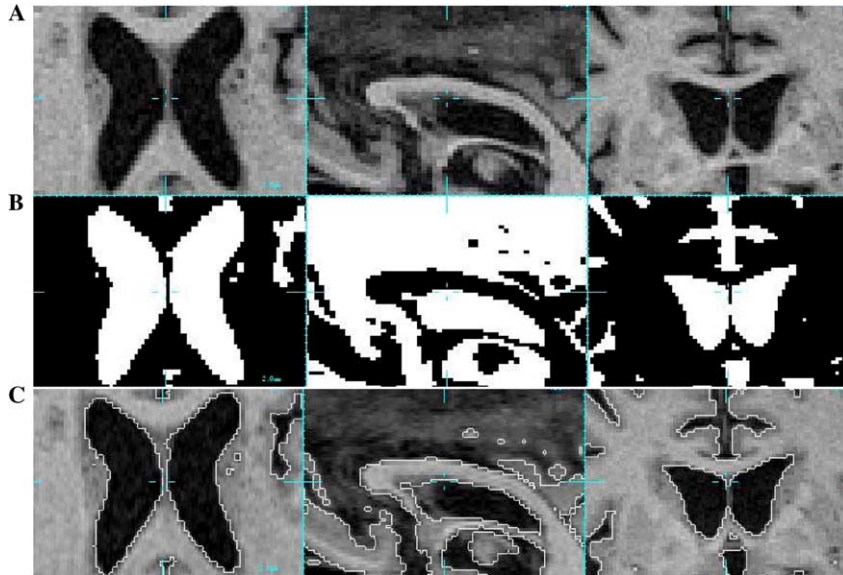


Fig. 7. Trans-axial (left), sagittal (middle), and coronal (right) slices through the: raw time point four image (A), final segmented CSF region (B), tissue-CSF contour over the time point four image (C).

Finally, Fig. 8 shows a comparison between our modified multi-phase level set model and the original multi-phase model (left column) and the effect of choosing the smoothness weights correctly to force constancy across time points (right column).

4. Conclusion and further work

In this paper, we propose two modifications to the multi-phase level set model for Mumford–Shah image segmentation. The first is an extension to the 4D case of the 4-phase piecewise constant active contour model without edges, introduced by Chan and Vese in [6,28] and used so far only in one, two or three dimensions. The advantage of this method is that the phases cannot produce vacuum or overlap, by construction. Also, the two level set functions can detect objects both with and without gradient, with weak edges, discontinuous boundaries or with holes and even with quite complex topologies like, for example, with triple junctions.

The second modification is the extension of this 4D multi-phase model to handle 4D images whose intensity changes in the temporal domain, by driving the boundary evolution from regional boundary information derived separately from each time step. In our model we have also made use of the known slow evolution of neurodegenerative conditions to introduce a greater smoothness penalty in the temporal direction, which provides robustness to low contrast tissue boundaries that occur due to the presence of white matter lesions.

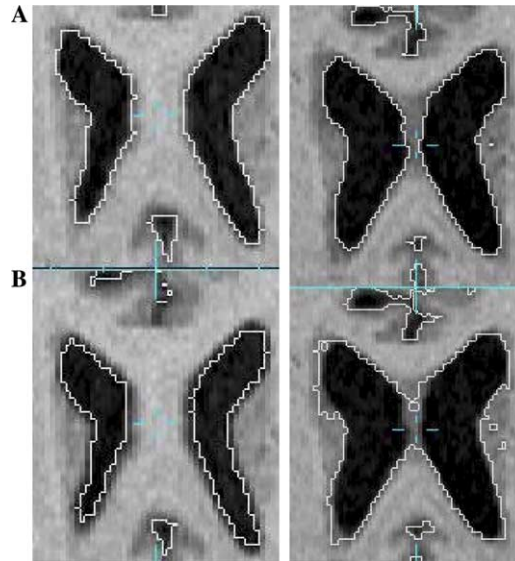


Fig. 8. Overlay of tissue-CSF contour onto trans-axial MRI slices showing the effects of the two proposed modifications to the multi-phase level set model (left column) and the effect of different temporal-spatial smoothness constraints (right column). In the left column we show results using our modified model (A) and the original, 4D multi-phase level set model (B). Note that the original formulation undersegments the CSF region of the ventricles at this time point, whereas our proposed model extracts a much more accurate tissue-CSF boundary. In the right column we show results using our modified model with equal spatial-temporal weights (B) and with $w_t = 8$ (A). Note particularly the errors in the contour location both in the mid-line and the left ventricular contour.

Because of the local character of this method, the initialization of the level set functions plays an important role in the correct segmentation of an image. Because the energy functional (2) is not convex, its local minimizer is not unique and therefore the numerical results can be sensitive to the initial positions of the two level set functions. Thus, it might happen that, for a given initialization, the algorithm may not converge to a global minimum. It is worthwhile to notice though that, even if the evolving hyper-surfaces are trapped at local minima, the reconstruction of the image may still be accurate.

Therefore, an investigation into making this model less sensitive to the initial positions of the two interfaces is worthwhile for the future. Also, further work is underway to evaluate the algorithm using a larger set of real image data with independent ground truth segmentations together with synthetic MR data.

Acknowledgments

This development work was primarily funded by Whitaker biomedical engineering grant RG-01-0115 and NIH Grant R01 MH65392. The authors wish to acknowl-

edge M. Weiner, B. Miller, and B. Jagust for access to imaging data provided through NIH Grants P01 AG12435, NIA P01 AG19724, P01 AA11493, and R01 AG10897. We thank the anonymous reviewers for useful comments and suggestions.

References

- [1] O. Amadieu, E. Debreuve, M. Barlaud, G. Aubert, Inward and outward curve evolution using level set method, in: *IEEE Proceedings 1999 International Conference on Image Processing*, 3 (1999), pp. 188–192.
- [2] C. Baillard, P. Hellier, C. Barillot, Segmentation of 3D brain structures using level sets and dense registration, in: *Proceedings of IEEE Workshop on Mathematical Methods and Biomedical Image Analysis, MMBIA-2000*, IEEE Comput. Soc. (2003), pp. 94–101.
- [3] V. Caselles, R. Kimmel, G. Sapiro, Geodesic active contours, *Int. J. Comput. Vis.* 22 (1) (1997) 61–79.
- [4] V. Caselles, F. Catté, B. Coll, F. Dibos, A geometric model for active contours in image processing, *Numerische Mathematik* 66 (1) (1993) 1–31.
- [5] V. Caselles, R. Kimmel, G. Sapiro, Geodesic active contours, *IEEE Int. Conf. Comput. Vis.* (1995), pp. 694–699.
- [6] T.F. Chan, L.A. Vese, Active contours without edges, *IEEE Trans. Image Process.* 10 (2) (2001) 266–277.
- [8] X. Han, C. Xu, M.E. Rettmann, J.L. Prince, Automatic segmentation editing for cortical surface reconstruction, in: *Proceedings of SPIE*, 4322 (2001), 194–203.
- [9] M. Kass, A. Witkin, D. Terzopoulos, Snakes: active contour models, *Int. J. Comput. Vis.* 1 (4) (1988) 321–331.
- [10] S. Kulkarni, B.N. Chatterji, Shape segmentation based on curve evolution using level sets, in: *Proceedings of the Eighth National Conference on Communications at Indian Institute of Technology Bombay*, 2002.
- [11] R. Malladi, J.A. Sethian, B.C. Vemuri, A topology independent shape modeling scheme, *Geometric Methods Comput. Vis.* II (1993) 246–256.
- [12] R. Malladi, J.A. Sethian, B.C. Vemuri, Evolutionary fronts for topology independent shape modeling and recovery, *Eur. Conf. Comput. Vis.* (1994) 1–13.
- [13] R. Malladi, J.A. Sethian, B.C. Vemuri, Shape modeling with front propagation: a level set approach, *IEEE-TPAMI* 17 (1995) 158–175.
- [15] T. McInerney, D. Terzopoulos, Deformable models in medical image analysis: a survey, *Med. Image Anal.* 1 (2) (1996) 91–108.
- [16] S. Osher, J.A. Sethian, Fronts propagating with curvature-dependent speed: algorithms based on Hamilton–Jacobi formulations, *J. Comput. Phys.* 79 (1988) 12–49.
- [17] S. Osher, R. Fedkiw, *Level set methods and dynamic implicit surfaces*, Springer Verlag, 2002.
- [18] S. Kichenassamy, A. Kumar, P. Olver, A. Tannenbaum, A. Yezzi, Gradient flows and geometric active contours models, *IEEE Int. Conf. Comput. Vis.* (1995) 810–815.
- [19] N. Paragios, R. Deriche, Geodesic active contours and level sets for the detection and tracking of moving objects, *IEEE Trans. Pattern Anal. Mach. Intell.* 22 (3) (2000) 266–280.
- [20] D. Peng, B. Merriman, S. Osher, H. Zhao, M. Kang, A PDE-based fast local level set method, *J. Computat. Phys.* 155 (1999) 410–438.
- [23] J.A. Sethian, *Level set methods and fast marching methods: evolving interfaces in computational geometry, fluid mechanics, computer vision, and materials science*, Cambridge University Press, 1999.
- [24] C. Studholme, D. Hill, D. Hawkes, An overlap invariant entropy measure of 3D medical image alignment, *Pattern Recogn.* 32 (1) (1999) 71–86.
- [27] J.K. Udupa, P.K. Saha, Fuzzy connectedness and image segmentation, *Proc. IEEE* 91 (10) (2003) 1649–1669.

- [28] L.A. Vese, T.F. Chan, A multiphase level set framework for image segmentation using the Mumford and Shah model, *Int. J. Comput. Vis.* 50 (3) (2002) 271–293.
- [29] L.A. Vese, Multiphase object detection and image segmentation, *Geometric Level set Methods in Imaging Vision and Graphics* (2003).
- [30] C. Xu, A. Yezzi Jr., J.L. Prince, On the relationship between parametric and geometric active contours, *The 34th IEEE Asilomar Conference on Signals, Systems and Computers I* (2000) 483–489.
- [31] C. Xu, A. Yezzi Jr., J.L. Prince, A summary of geometric level-set analogues for a general class of parametric active contours and surface models, in: *Proceedings of the 1st IEEE Workshop on Variational and Level Set Methods in Computer Vision*, 2001, pp. 104–111.